Natural Resources Canada
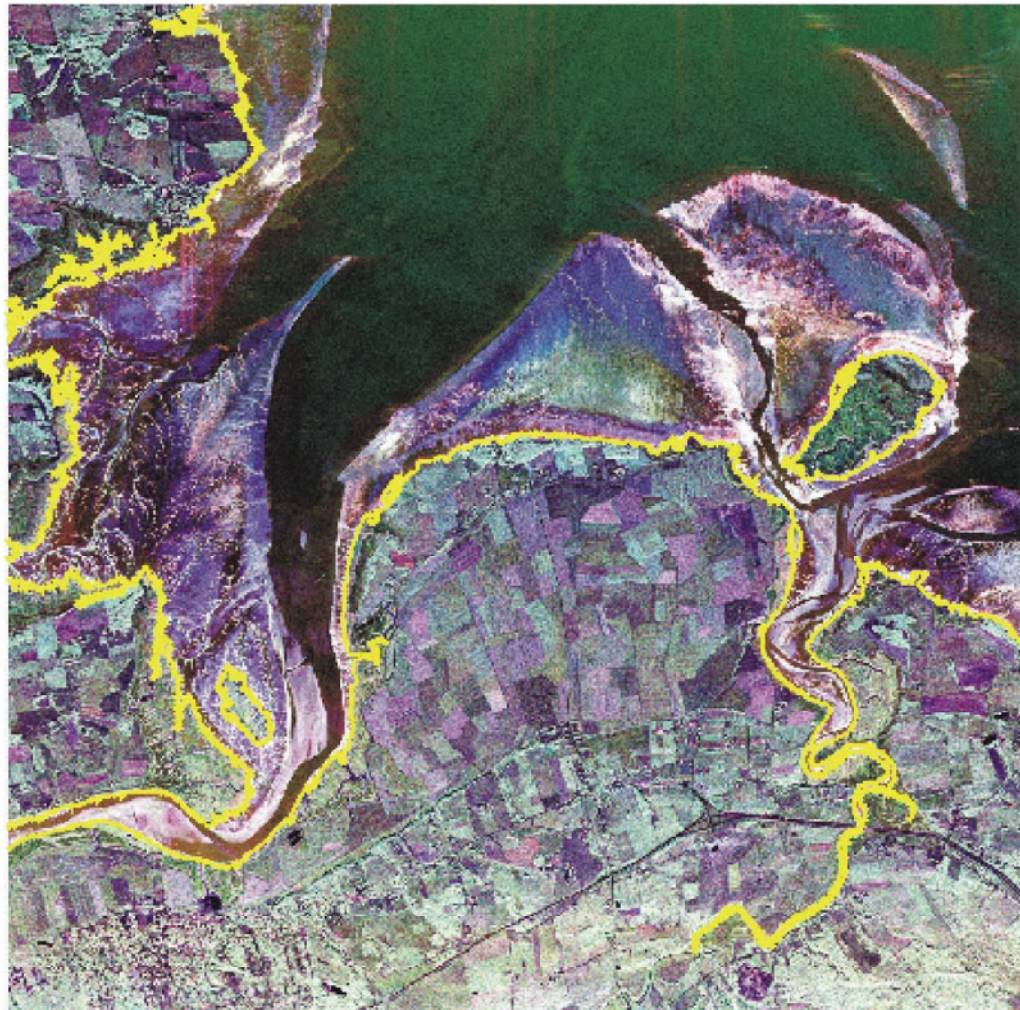
Ressources naturelles Canada

Geomatics Canada

POLARIMETRIC SAR FOR GEOMORPHIC MAPPING IN THE INTERTIDAL ZONE, MINAS BASIN, BAY OF FUNDY, NOVA SCOTIA

Chris Hugenholtz
Joost van der Sanden

November 2001

Canada Centre for Remote Sensing

SUMMARY

The purpose of this study was to assess the potential of airborne polarimetric Synthetic Aperture Radar (SAR) data for geomorphic mapping of intertidal terrain. The study is part of ongoing applications development research at the Canada Centre for Remote Sensing (CCRS) in preparation for the launch of RADARSAT-2 in 2003. Calibrated polarimetric Convair-580 SAR data were acquired during low tide conditions over the southern Bight of Minas Basin, Bay of Fundy, Nova Scotia, in November 1999. It is shown that there is a significant improvement in geomorphic target identification and discrimination when fully polarimetric SAR data are used. Qualitative analysis of the SAR power images reveals the relative importance of surface and vegetation scatter in the intertidal terrain. Strong backscatter contrasts in the linear polarizations enabled delineation of the boundaries between various tidal sub-environments. The cross-polarized channel return (σ°_{HV}) was the optimal polarization for delineating the mean high water line. The HH-polarized channel return (σ°_{HH}) was the optimal polarization for delineating the mean low water line and enabled differentiation of intertidal sediment classes. Comparison of co-polarized polarimetric response plots from different tidal sub-environments with previous studies reveals the importance of surface roughness as the dominant target scattering mechanism in the intertidal zone. An unsupervised classification of target scattering behaviour shows good agreement with the known distribution of intertidal vegetation and sediment characteristics.

1. INTRODUCTION

Conventional geomorphic mapping of the intertidal zone from land-based (i.e., geodetic) and ship-based (i.e., echo-sounding) surveys is extremely time consuming and expensive. Furthermore, intertidal zones, particularly those characterized by extensive mud deposits, are difficult to measure because of their inaccessibility and the dangers posed by the mud and tides. Increasingly, remote sensing is being used as an alternative method for rapidly delineating and classifying intertidal areas (e.g., Yates et al., 1993; Lohani and Mason, 1999; Rainey et al., 2000). These data are critical for monitoring spatially distributed sedimentary and biologic processes in intertidal zones and provide important insight into ecosystem structure and dynamics. The potential for systematic coverage from satellite remote sensing platforms and the synoptic information inherent in these data can improve our understanding of the impacts of global change, particularly related to sea-level changes.

A number of satellite and airborne remote sensing studies have attempted to map the intertidal zone, focussing primarily on the nature and distribution of intertidal sediments and landforms. Studies involving optical platforms (e.g., Bartholdy and Folving, 1986; Yates et al., 1993; Rainey et al., 2000) have contributed to our understanding of intertidal ecology, morphodynamics and pollution processes. However, systematic coverage with optical devices is problematic because atmospheric phenomena such as clouds effectively mask certain regions during image acquisition. These effects limit the usefulness of optical devices, especially in cloud- and fog-prone coastal areas.

Radar platforms provide a strategic advantage over optical platforms, particularly for operational users, by enabling systematic coverage (satellite platforms) and different information (i.e., structural). Studies in intertidal areas using SAR have used both single-frequency/single-polarization data (e.g., Tittley, 1990; Tittley and Werle, 1997) and multi-frequency/multi-polarization data (Melsheimer et al., 1998; Tanck et al., 1999). In contrast to the single-polarization data currently available from satellite platforms (e.g., Radarsat, ERS), fully-polarimetric SAR data provides information on the complete scattering matrix of imaged targets. These data are particularly well suited for studies on structural elements in the intertidal zone. Geomorphic targets of interest in the intertidal zone include: sediment type, tidal creeks, ephemeral bedform features, sandbars, bedrock outcrops, and vegetation.

In this study we use C-Band fully-polarimetric SAR imagery collected aboard Environment Canada's CV-580 aircraft over the southern Bight of the Minas Basin, Bay of Fundy, Nova Scotia, Canada. The data were collected during low-tide conditions on November 10, 1999 in an east-to-west direction. The purpose of the study was to explore the potential of airborne POL-SAR to distinguish various geomorphic targets in the intertidal zone as an analogue for future POL-SAR satellites such as RADARSAT-2.

2. BACKGROUND

2.1 Polarimetric SAR (POL-SAR)

Polarimetric SAR (POL-SAR) is a technology that exploits the polarized nature of electromagnetic waves in order to extrapolate multi-dimensional information from imaged targets. The polarization of a wave is the description of the spatial orientation of the electric

vector for a given wave. In single-polarization SAR's the electric field is recorded as either H- or V-polarized waves and a single scattering coefficient is measured for thousands of points in the scene. In this configuration SAR's only measure a scalar quantity and loose the polarization properties of the reflected wave. In fully polarimetric SAR's the polarization of the reflected wave is measured as a vector quantity and the polarization signature of every resolution cell is recorded.

The electric field (E) of a multi-polarized wave consists of the vector sum of the H- and V-polarized electric field components. The phase difference between these two components results in a wave having either a linear, elliptical or circular polarization. The rotation direction of the wave is defined by two parameters: ellipticity angle (χ) and orientation angle (Ψ). Ellipticity ranges between -45º (right-handed) and 45º (left-handed). For linearly polarized waves, χ is equal to 0º. For circularly polarized waves, χ is equal to ± 45º. The orientation angle is either 0º or 180º for H-polarization and 90º for V-polarization.

Fully polarimetric SAR data provides the 2 × 2 target scattering matrix (also referred to as the Sinclair scattering matrix):

$$S = \begin{pmatrix} S_{HH} & S_{HV} \\ S_{VH} & S_{VV} \end{pmatrix}$$

(eq. 1)

Knowledge of the scattering matrix permits calculation of the received power for any combination of transmit and receive antennas and is referred to as polarization synthesis (van Zyl and Zebker, 1990). Reciprocity dictates that $S_{HV} = S_{VH}$ for monostatic polarimeters where the target is not affected by Faraday rotation.

POL-SAR data is necessarily large and often beyond the processing capabilities of many users. For reasons of data handling efficiency, individual measurements are combined to form the Stokes matrix or covariance matrix which preserve the polarization, amplitude and phase information (cf. van Zyl and Zebker, 1990; Boerner et al., 1998). The state of polarization of a wave can be expressed in terms of the Stokes parameters:

$$S_1 = S_o \cos (2\psi) \cos (2X)$$ (eq. 2a)

$$S_2 = S_o \sin (2\psi) \cos (2X)$$ (eq. 2b)

$$S_3 = S_o \sin (2X)$$ (eq. 2c)

where S_o is the radius of the Poincaré sphere and is proportional to the total power in the wave (van Zyl et al., 1987).

The Stokes matrix uses the four Stokes parameters from the transmitted wave:

$$\begin{pmatrix} S_0 \\ S_1 \\ S_2 \\ S_3 \end{pmatrix}^R = [R][\widetilde{R}][M] \begin{pmatrix} S_0 \\ S_1 \\ S_2 \\ S_3 \end{pmatrix}^T$$

(eq. 3)

where the superscripts T and R represent the transmit and received waves respectively. The Stokes matrix $[M]$ can be expressed as:

$$[M]=[\widetilde{R}]^{-1}[W][R]^{-1} \qquad\qquad \text{(eq. 4)}$$

where ˜ denotes matrix transpose and $[W]$ is defined by:

$$[W]=\begin{pmatrix} S_{HH}S_{HH}^{*} & S_{HV}S_{HV}^{*} & S_{HH}S_{HV}^{*} & S_{HV}S_{HH}^{*} \\ S_{VH}S_{VH}^{*} & S_{VV}S_{VV}^{*} & S_{VH}S_{VV}^{*} & S_{VV}S_{VH}^{*} \\ S_{HH}S_{VH}^{*} & S_{HV}S_{VV}^{*} & S_{HH}S_{VV}^{*} & S_{HV}S_{VH}^{*} \\ S_{VH}S_{HH}^{*} & S_{VV}S_{HV}^{*} & S_{VH}S_{HV}^{*} & S_{VV}S_{HH}^{*} \end{pmatrix} \qquad\qquad \text{(eq. 5)}$$

where * denotes the complex conjugate and:

$$R=\begin{pmatrix} 1 & 1 & 0 & 0 \\ 1 & -1 & 0 & 0 \\ 0 & 0 & 1 & 1 \\ 0 & 0 & -i & i \end{pmatrix} \qquad\qquad \text{(eq. 6)}$$

The assumption of reciprocity causes $[M]$ to be symmetrical and makes this 4 x 4 matrix fully describable with just ten independent elements. These ten parameters can be used to derive various scene statistics:

$$M_{11} = \tfrac{1}{4}(|S'_{HH}|^2 + |S'_{VV}|^2 + 2|S'_{HV}|^2) \qquad\qquad \text{(eq. 7a)}$$

$$M_{12} = \tfrac{1}{4}(|S'_{HH}|^2 - |S'_{VV}|^2) \qquad\qquad \text{(eq. 7b)}$$

$$M_{13} = \tfrac{1}{2}Re(S'^{*}_{HH}S'_{HV} + S'^{*}_{VV}S'_{HV}) \qquad\qquad \text{(eq. 7c)}$$

$$M_{14} = \tfrac{1}{2}Im(S'^{*}_{HH}S'_{HV} - S'^{*}_{VV}S'_{HV}) \qquad\qquad \text{(eq. 7d)}$$

$$M_{22} = \tfrac{1}{4}(|S'_{HH}|^2 + |S'_{VV}|^2 - 2|S'_{HV}|^2) \qquad\qquad \text{(eq. 7e)}$$

$$M_{23} = \tfrac{1}{2}Re(S'^{*}_{HH}S'_{HV} - S'^{*}_{VV}S'_{HV}) \qquad\qquad \text{(eq. 7f)}$$

$$M_{24} = \tfrac{1}{2}Im(S'^{*}_{HH}S'_{HV} + S'^{*}_{VV}S'_{HV}) \qquad\qquad \text{(eq. 7g)}$$

$$M_{33} = \tfrac{1}{2}|S'_{HV}|^2 + \tfrac{1}{2}Re(S'^{*}_{HH}S'_{VV}) \qquad\qquad \text{(eq. 7h)}$$

$$M_{34} = \tfrac{1}{2}Im(S'^{*}_{HH}S'_{VV}) \qquad\qquad \text{(eq. 7i)}$$

$$M_{44} = \tfrac{1}{2}|S'_{HV}|^2 - \tfrac{1}{2}Re(S'^{*}_{HH}S'_{VV}) \qquad\qquad \text{(eq. 7j)}$$

2.2 Backscatter properties of tidal sub-environments

The differential radar cross-section (σ^o) is a response to both surface and system parameters. Surface parameters include surface roughness (i.e., centimeter to meter scale) and soil dielectric properties attributable to mineralogy, grain size, soil moisture, and soil structure. System parameters include wavelength (λ), look angle and direction, incident angle (θ^o_{inc}), and polarization. Radar interaction with surficial deposits can occur at two levels: (1) according to the roughness of the imaged ground (microtopography) and (2), single- or double-bounce interactions with large individual objects, from pebbles to boulders, whose size is similar or greater than the radar wavelength (Boerner et al., 1998). Linear co-polarized microwaves (i.e., HH and VV) are generally more sensitive to the orientation of the target relative to the transmitted polarization whereas cross-polarized waves (i.e., HV) are more sensitive to multiple scatter at the surface and, if penetration occurs, volume scattering from the subsurface.

The intertidal zone in macrotidal basins is typically characterized by gentle topography with broad sand/mudflats dissected by tidal creeks (e.g., Severn River, United Kingdom; San Sebastian Bay, Argentina; and the Bay of Fundy, Canada). The backscatter coefficient from these broad intertidal areas is largely a response to variations in aquatic vegetation, grain size, moisture content and surface roughness. In recent SAR studies on intertidal sediments, Melcheimer et al. (1998) and Tanck et al. (1999) explored multi-frequency/multi-polarization SIR-C/X-SAR images from the Wadden Sea at low tide. Results from these studies indicated that the radar backscatter was mainly controlled by the surface roughness attributable to ebb and tide current structures rather than soil moisture.

3. STUDY AREA

Minas Basin is a large macrotidal basin located in the upper reaches of the Bay of Fundy (Figure 1). The area is characterized by one of the largest semidiurnal tidal ranges in the world. Average tidal amplitude is 11.5 m, ranging up to 15 m (Yeo and Risk, 1981) with a period of oscillation of 6.29 hours (approximating a semidiurnal period). Tidal velocities are extreme, reaching up to 11 knots and generally 3-4 knots in the open basin (Middleton, 1972). Due to the Coriolis effect, the flooding tide moves along the southern margin of the Bay, while the ebb moves along the northern margin, resulting in a counter-clockwise tidal system (Swift and McMullen, 1968).

The entrance to Minas Basin from the Bay of Fundy (Minas Passage) is constricted by Cape Split, a formation of resistant Triassic basalts (Swift and McMullen, 1968), the shape of which is a result of the Fundy Syncline plunging westward through Scots Bay (Middleton, 1972). This narrow passage plays a crucial role in amplifying the tidal range. Petrographic studies show that the deeper parts of the Basin are underlain by a diamicton overlying Triassic bedrock. The diamicton is thought to have originated from the late Quaternary and is overlain by stratified deposits of fluvial and marine outwash sediments (Swift and McMullen, 1968).

Tidal fluxes play an important role in the sedimentary regime of the Minas Basin. Tides control the distribution of sediment and the morphology of ephemeral features such as migrating sand wave fields. Because of the large tidal range in the Basin, the intertidal zone is an extremely extensive ecosystem (Thomas, 1977). Bousfield and Leim (1960) indicate that more than one-third of the bottom is exposed at low tide.
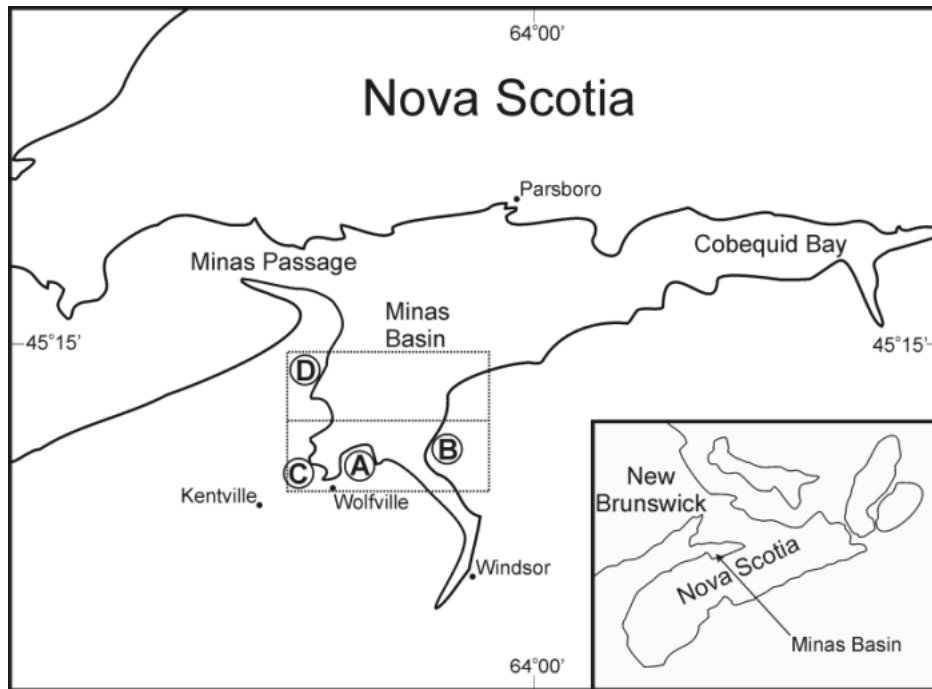
FIGURE 1: Location of study area. Four distinct regions are identified: (A) South, (B) Southeast, (C) Southwest, (D) Northwest. Location of POL-SAR image specified by box.

The intertidal sediment distribution in the study area can be separated into four major regions (Figure 1): southern, southeastern, southwestern and northwestern. The least extensive intertidal zone is found along the shore of the northwestern side of the basin, corresponding to the location of highly erosive Triassic sandstone cliffs and strong anisotropic ebb and tide currents. Similar anisotropic currents occur along the southeast region at the mouth of the Avon River, but the intertidal zone is slightly greater in extent and there are numerous limestone bedrock outcrops with irregularly modulated expressions (karstic). More extensive intertidal areas are found along the southern and southwestern shores where the current velocities decrease substantially, enabling deposition of fine sediment and resulting in extensive mud and sand deposits and salt marshes. One particularly interesting feature at the southern intertidal mudflat is the widespread occurrence of boulders in the muddy sediment (Figure 2). According to observations by Knight and Dalrymple (1976) these boulders represent ice-rafted material deposited during winter conditions.

4. DESCRIPTION OF DATA

The POL-SAR data used in this study were collected by Environment Canada's CV580 aircraft in an east-west direction on November 10, 1999, between 12:06:23.648002 and 12:12:10.74000 UTC. The SAR onboard the CV580 (Livingstone et al., 1995) was developed by the Canada Centre for Remote Sensing (CCRS). The data consist of radiometrically corrected fully-polarimetric data in C-Band (λ = 5.6 cm), Single-look Complex (SLC), 32bit floating point format. The flying altitude was approximately 6015 m and the

resolution of the data was approximately 4 m in slant range by 0.42 m in azimuth. A series of nine corner reflectors were used for calibration during image acquisition.

A   **B**
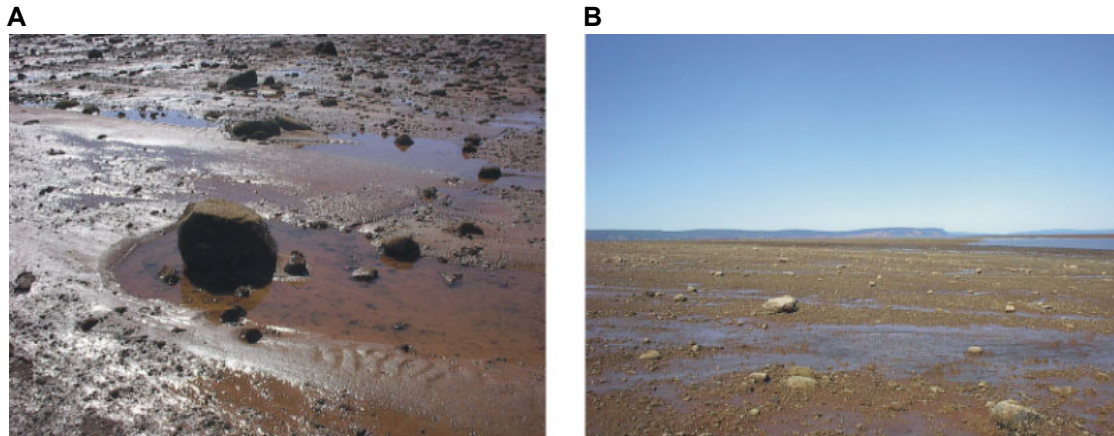
FIGURE 2: A) Photograph of a large ice-rafter boulder at Evangeline Beach mudflat. Note the large water-filled scour mark around the boulder. The boulder height is approximately 0.5 m. B) Photograph of boulders and gravel along eastern margin of Evangeline Beach mudflat.

5. METHODS

5.1 Field Methods
An initial analysis of the intertidal zone in the SAR image was done prior to field visits in order to identify areas of interest. Field observations were made in June and September 2001 under similar conditions to when the CV580 SAR data were acquired. Surface characteristics of each terrain type were recorded in an effort to understand and identify the features that control the backscatter observed in the SAR image. The SAR image was used to guide the field studies in different tidal sub-environments. The primary field method consisted of photographing various intertidal features present within each region. As a result of accessibility problems and the dangers imposed by the intertidal mud deposits, only a few sub-environments could be visited.

5.2 Data Processing
The complex data were provided at the POLGASP level of processing (Hawkins et al., 1999). The data were phase corrected, azimuth focused and motion compensated. Raw file dimensions were 65,000 pixels in azimuth and 4,096 pixels in slant range. Initially, the data were processed with a series of independent FORTRAN-based routines to transform the complex data into PCI (.pix) format and extract various scene statistics. Later, the data were entered into polarimetric analysis software (PWS1.1) developed by R. Touzi and F. Charbonneau (CCRS). This software enabled extraction of amplitude images, polarization response plots, and phase difference images. Image visualisation was done on 32-bit imagery in PCI. Image processing involved contrast enhancements and filtering to better distinguish various terrain types.

6. IMAGE ANALYSIS AND INTERPRETATION

Image analysis consisted of visual interpretation of the linear polarization power images and the composite image. Due to the assumption of reciprocity (i.e., $S_{HV} = S_{VH}$), only the HV cross-polarized image was examined. A total of five sub-regions were selected for further analysis which comprise distinct tidal sub-environments in the Minas Basin. The locations of the sub-regions are shown in Figure 3. They are: a) Middle Ground sandbar, b) bedrock outcrops along the eastern shore zone (Scotch Rocks), c) a large mudflat near Evangeline Beach, d) the salt marshes of the Canard and Habitant Rivers, and e) the mudflats of the Canard River Estuary (Starr's Pt.).

6.1 Middle Ground sandbar
Middle Ground (Canadian Hydrographic Service, 1972) is a large intertidal sandbar located at the mouth of the Avon River (Figure 3). When exposed at low tide, the bar is approximately 5.6 km in its longest dimension (a-axis) and 0.9 km wide (b-axis). The a-axis follows the local anisotropic current regime. A seismic profile in 1975 by the Bedford Institute of Oceanography determined that Middle Ground contains a bedrock core. The sediment and bedform distribution have been described by Lambiase (1980). The author distinguishes six principle bedform zones on the bar which are characterised by four bedform class configurations: sinuous and linear megaripples, linguoid ripples, and plane bed. The megaripple bedforms are on the order of 0.5 m in wave height and 10 m in wavelength. The ripple bedforms are 0.05 m in height and 0.3 m in wavelength.
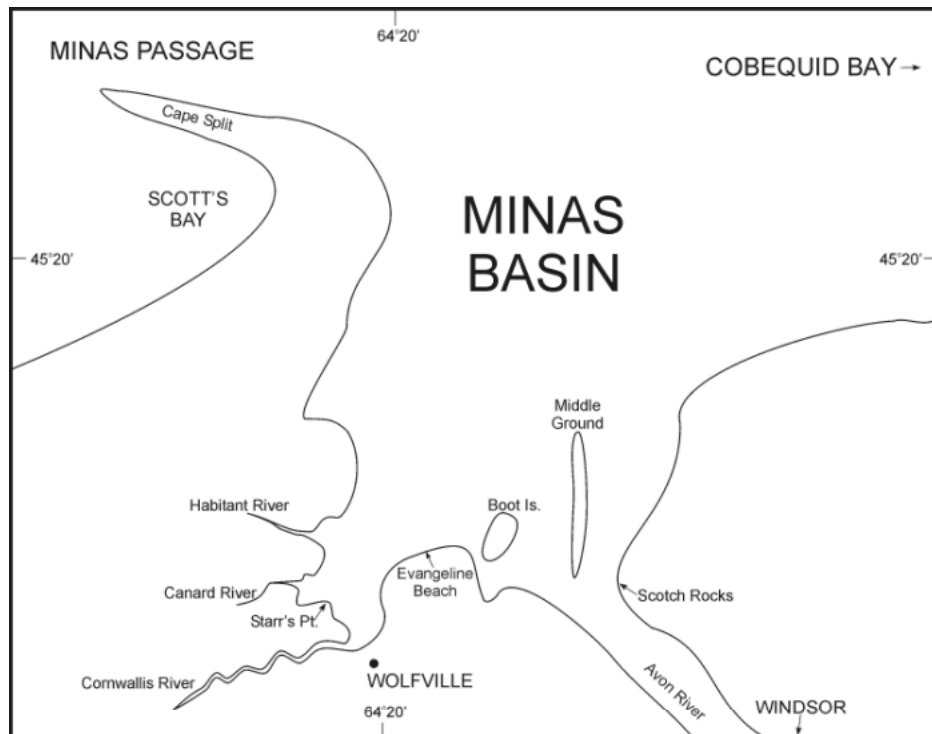
**FIGURE 3:** Location of key sub-regions.

Figure 4 shows the three polarizations and a composite image of Middle Ground sandbar. The composite image shows that the airborne SAR is capable of resolving the main structural sediment pathways of the sandbar (cf. Lambiase, 1980). Distinction can be made between various features including the main crest of the sandbar, the linear megaripples along the southern portion of the bar, and the larger linguoid megaripples to the north. Comparison of the three individual polarization power images indicates some difference in the terrain backscatter response. Bedform structure and sediment pathways are well pronounced in all three polarizations, however, the VV-polarization reveals more of the small-scale bedform structures. In comparison, the HH-polarization image provides a better discrimination of the large megaripples because the horizontally transmitted electric vector couples more effectively than VV to the horizontal orientation of the ripples. A common element to all-three polarization power images is a well-defined bright region (high backscatter) on the western margin of the bar. According to Lambiase (1980) this area does not correspond to any particular bedform feature. Unfortunately, due to accessibility problems Middle Ground could not be accessed for field verification. It is possible that the high return is the result of Bragg scattering from periodically spaced ripples formed during the latter stages of the ebb. However, It is more likely that the high return is the result of scattering from ice-rafted boulders or gravels, since these are common in other portions of the basin (cf. Knight and Dalrymple, 1976).

Examination of the backscatter values over various regions on the sandbar supports the initial visual interpretation. Overall, the highest average backscatter occurs in the VV-polarization (-21.1 dB) followed by the HH- (-25.6 dB) and HV-polarizations (-37.6 dB). The greatest variability in backscatter occurs in the HH- and HV-polarizations, indicating why the megaripples are best visually discriminated in these power images. Comparison of three-dimensional surface plots of the backscatter from the megaripples provides an additional visualization of the improved imaging potential of the HH- and HV-polarizations for large bedforms oriented more or less parallel to the radar track (APPENDIX 1A).

6.2 Eastern shore bedrock outcrops

The eastern shore is characterized by extensive sand/mudflats and a series of Triassic limestone bedrock outcrops. These rocks are comparably more resistant to erosion than the red Triassic sandstone common in other areas in the Basin and have formed a karstic topography in the region near Scotch Rocks (Figure 3). The limestone is a member of the Windsor Group which also contains sandstone, siltstone, dolostone, anhydrite and gypsum (Bell, 1960). Air photos indicate that the bedrock surface is extremely distorted along the shore zone, resulting in a modulated appearance in some areas with sand deposits filling the depressions of the modulations in the intertidal zone.

The three-polarization power images and composite image of Scotch Rocks are shown in Figure 5. Bedrock produces a high radar return relative to the surrounding intertidal sands with the greatest contrast occurring in the HV- and HH-polarization images, respectively. The modulations in the bedrock are clearly distinguished in all three polarization images. The HH image produces the best contrast with the sand in the bedrock troughs. These observations are supported by three-dimensional plots of the backscatter versus incident angle (θ°_{inc}) and azimuth distance (APPENDIX 1B). These plots show that the VV-polarization is more sensitive to the sand and produces a higher backscatter and subsequently a higher return from the bedrock troughs. In comparison, both the HH-polarization and to a lesser extent the HV-polarization produce better backscatter contrasts because of much lower backscatter from the troughs.
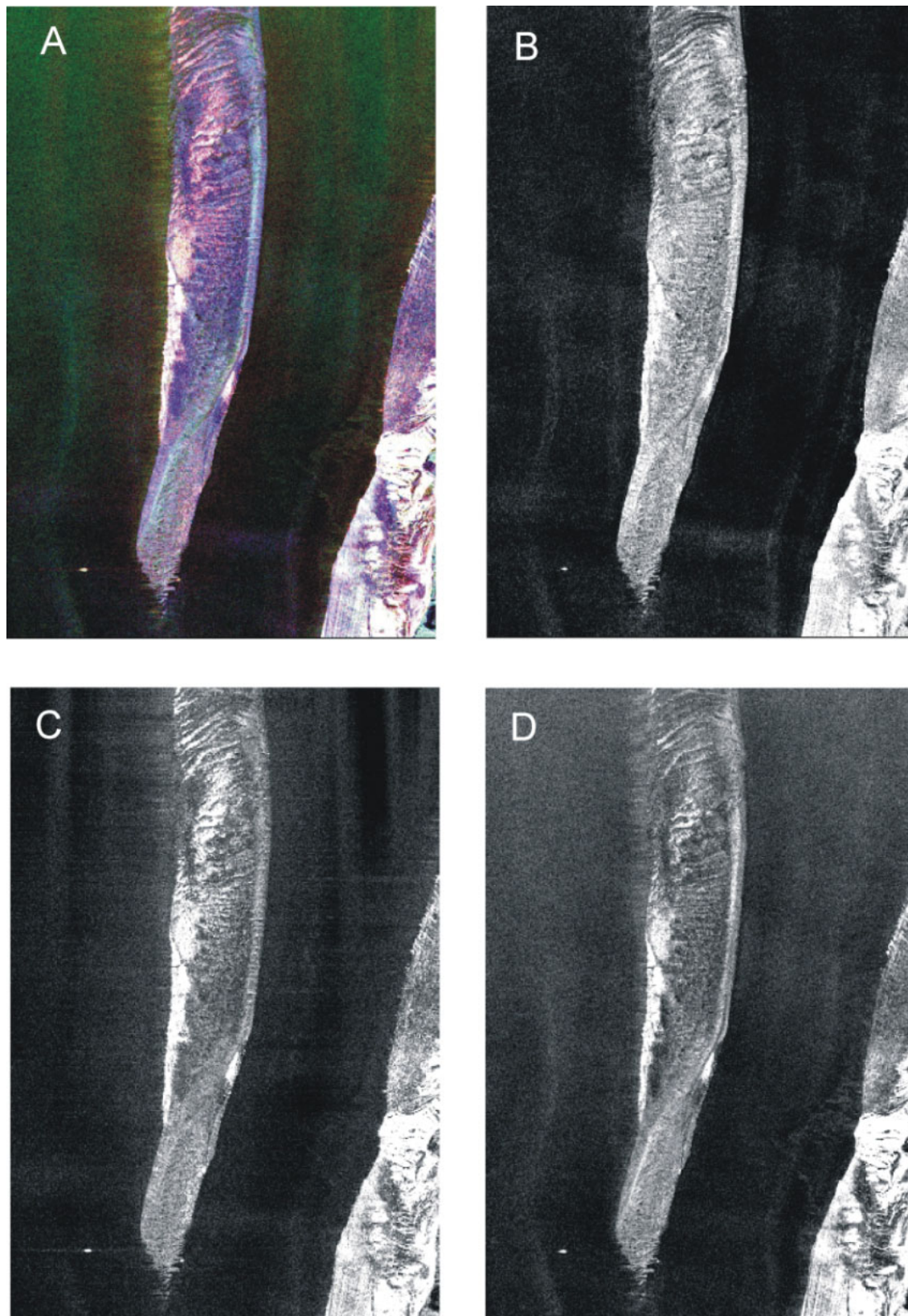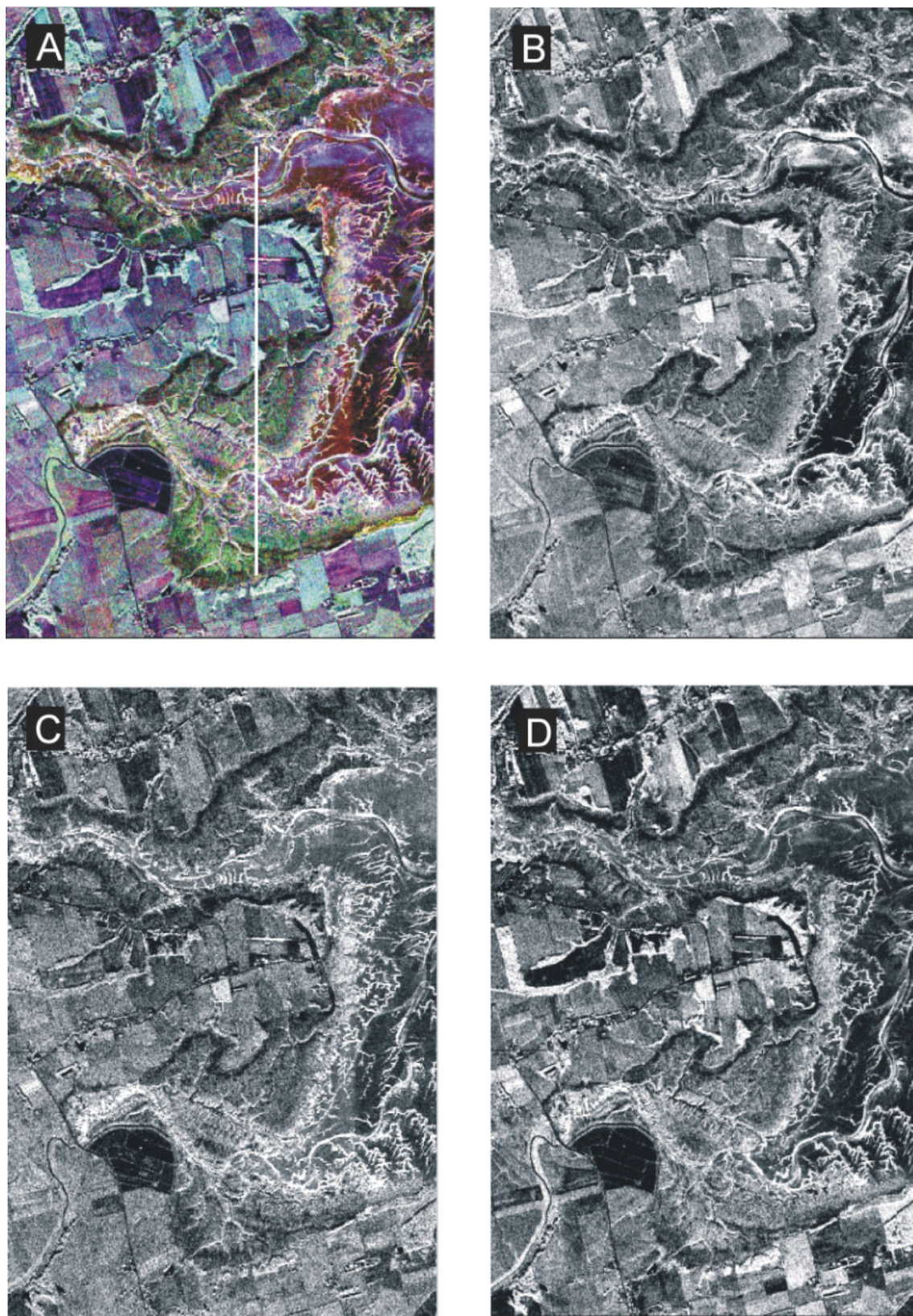
FIGURE 4: RGB color composite (R-HH, G-HV, B-VV) and three linear polarizations (VV, HH, and HV, respectively) for Middle Ground sandbar. A) RGB, B) VV, C) HH, and D) HV.
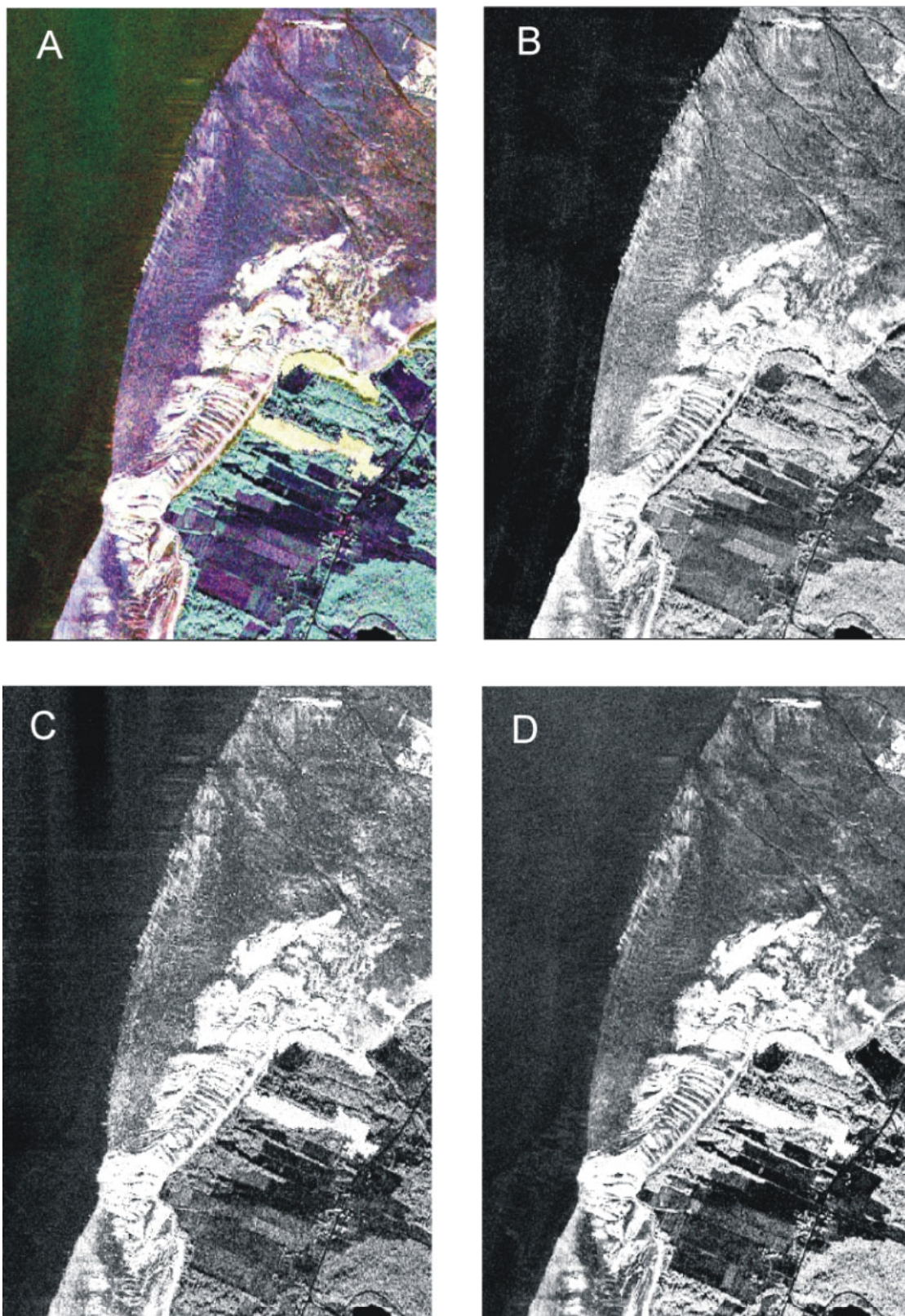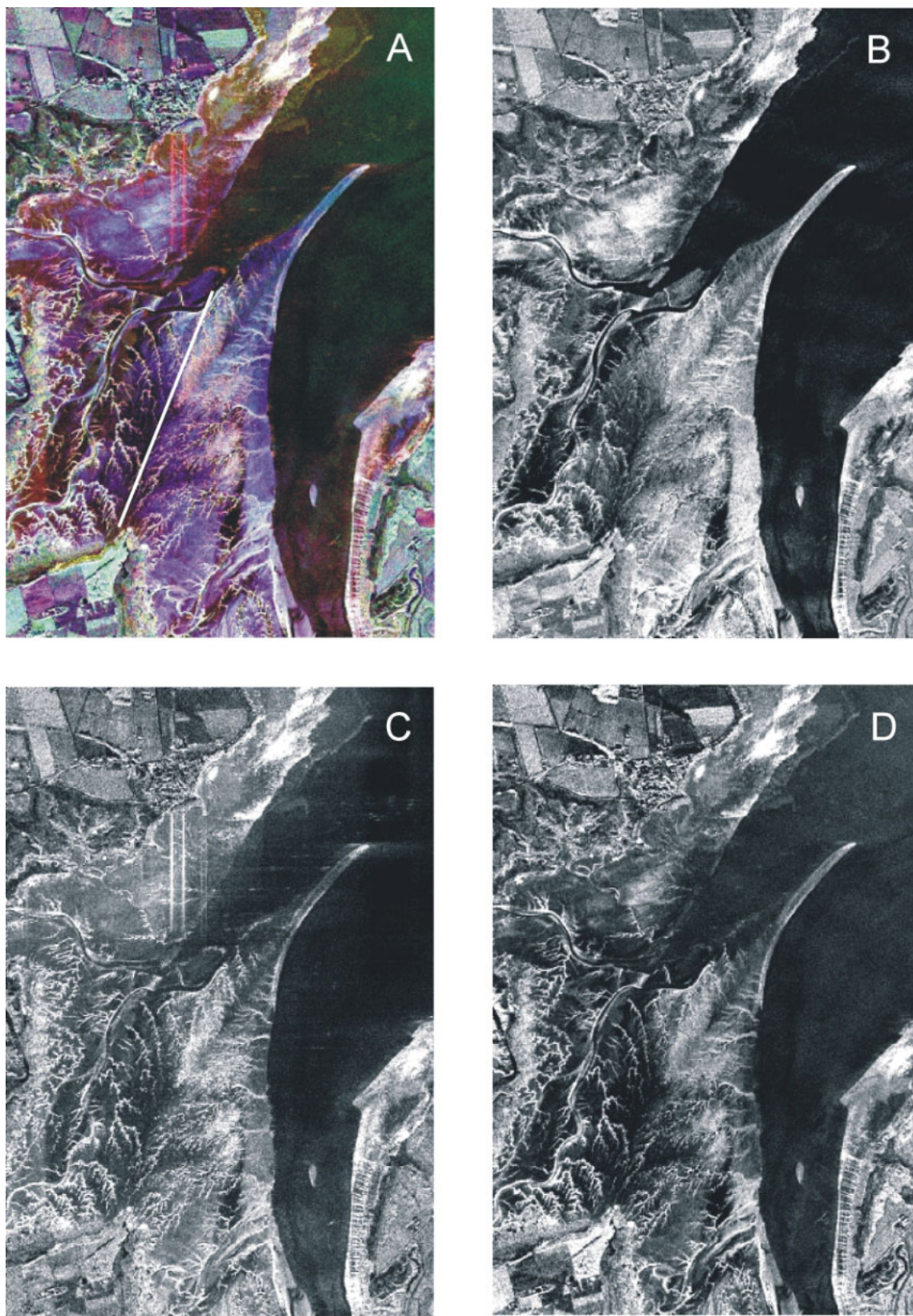
FIGURE 5: RGB color composite (R-HH, G-HV, B-VV) and three linear polarizations (VV, HH, and HV, respectively) for Scotch Rocks. A) RGB, B) VV, C) HH, and D) HV.
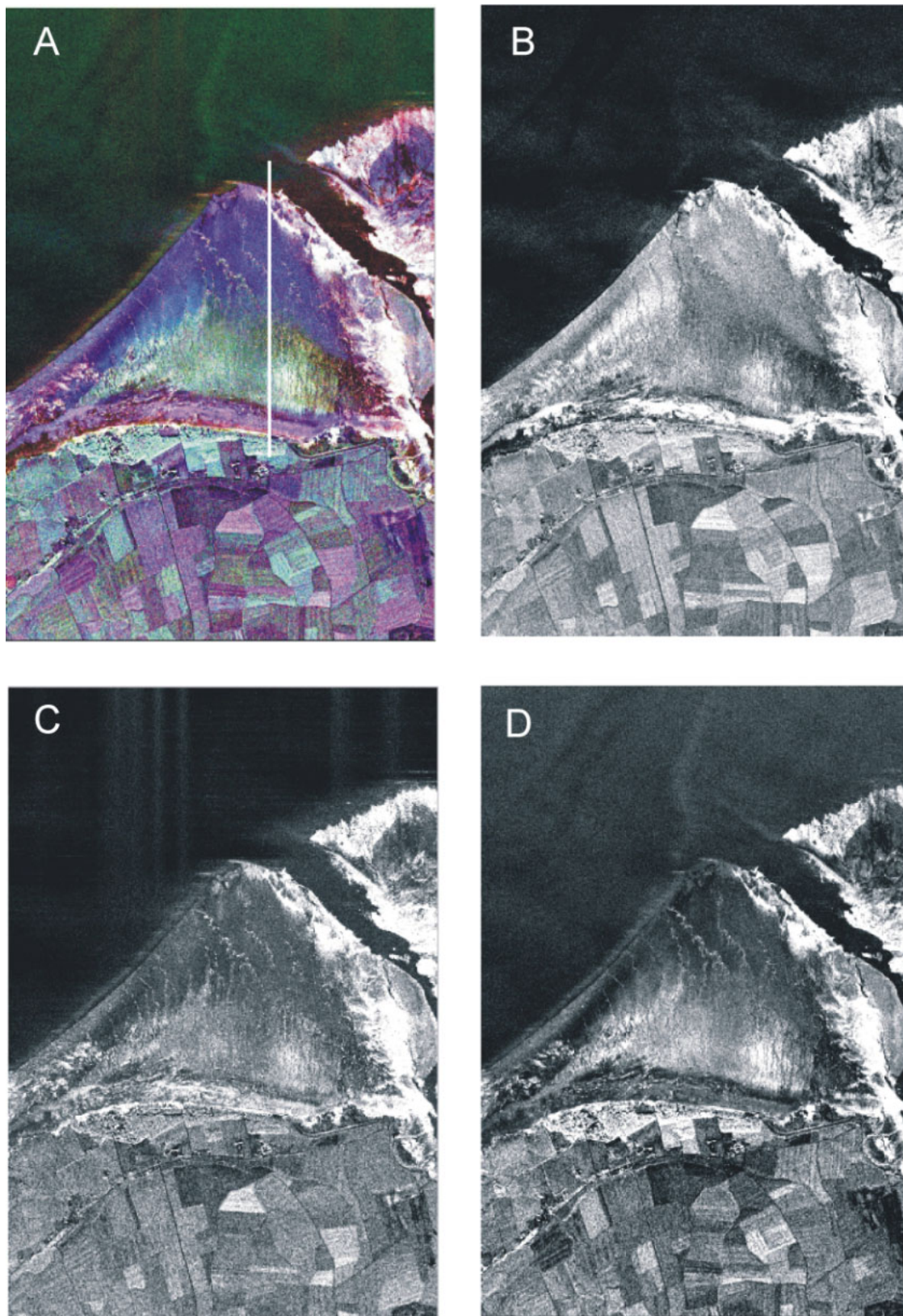
FIGURE 6: RGB color composite (R-HH, G-HV, B-VV) and three linear polarizations (VV, HH, and HV, respectively) for Evangeline Beach mudflat. A) RGB, B) VV, C) HH, and D) HV.

FIGURE 7: RGB color composite (R-HH, G-HV, B-VV) and three linear polarizations (VV, HH, and HV, respectively) for Canard and Habitant salt marshes. A) RGB, B) VV, C) HH, and D) HV.

FIGURE 8: RGB color composite (R-HH, G-HV, B-VV) and three linear polarizations (VV, HH, and HV, respectively) for Starr's Point mudflat. A) RGB, B) VV, C) HH, and D) HV.

An evaluation of the average backscatter values from a portion of the modulated bedrock indicates that VV has the highest average backscatter (-18.0 dB) followed closely by HH (-19.6 dB) and HV (-29.3 dB), respectively. The greatest variability in sigma naught occurs in the HV- and HH-polarizations (S.D. values are 6.2 and 5.7, respectively). The majority of this variability is related to the reduction of backscatter from the sand in between the bedrock modulations and indicates why the HH- and HV-polarizations provide the best contrast between bedrock and sand. It should be noted that σ°_{HH} often exceeds σ°_{VV} over the bedrock because the horizontal radar waves couple more effectively with the orientation of the bedrock modulations.

6.3 Intertidal mudflat at Evangeline Beach

An extensive intertidal flat occurs at Evangeline Beach (Figure 3). The central portion of the flat is characterized by a relatively smooth gentle slope (1-2º), with no significant tidal creeks or large-scale ripple forms. The substrate varies considerably across the flat. Sediment types range from friable sandstone to muds, sands and gravels. Small drainage channels and ice-rafted boulders are scattered across the flat. A large channel, referred to as the Guzzle, separates the flat from Boot Island. Extensive gravel and boulder deposits occur along the sides of the Guzzle (Figure 2B).

The multi-polarized composite image reveals some strong contrasts in the radar return (Figure 6). The extensive green area indicates the dominance of cross-polarized return which would be expected from volume or mutliple scattering as the result of greater depolarization. Yet there is no vegetation in this area of the mudflat. Field observations indicate that this surface consists primarily of friable sandstone that may have sufficient porosity to account for the depolarization. The precise depolarizing mechanism requires further study.

The white areas along the eastern margin of the mudflat indicate strong backscatter from all polarizations. Field observations confirm that the high backscatter is from gravel deposits and ice-rafted boulders (Figure 2). A backscatter transect across the entire flat for an incident angle range of 60 to 66º reveals some significant variations in the backscatter coefficient associated with different intertidal features (Figure 9). Average backscatter values over the flat show that the strongest return is from the VV-polarization (-22.5 dB) followed by HH (-31.3 dB) and HV (-37.7 dB), respectively. However, there is more variability in the HH-polarization (S.D. values: HH = 7.5, HV = 6.4 and VV = 5.0). The backscatter values from the HH- and VV-polarizations are nearly symmetric over the deciduous forest along the shoreline, but they diverge rapidly at the edge of the near-shore gravel facies (where $\sigma^{\circ}_{VV} > \sigma^{\circ}_{HH}$). The cross-polarization backscatter drops much more than the linear polarizations from land into the intertidal zone. This is the result of high σ°_{HV} attributable to depolarization from the deciduous forest along the shoreline and the lack of significant depolarization (i.e., low σ°_{HV}) in the intertidal zone. The contrast in HV backscatter between land and the intertidal zone indicates that HV is the optimum polarization for delineating the mean high water line in POL-SAR imagery taken at low tide. It should be pointed out that this is not necessarily the case at the mean low waterline because the contrast between the two media is much lower than the co-polarizations.

### 6.4 Salt marshes of the Canard and Habitant Estuaries

Salt marshes in the Minas Basin are raised mudflats which have formed in sheltered intertidal areas and have been stabilized by vegetation colonization. Examples of salt marshes in Minas Basin are shown in Figure 10. The sediment is dominated by fine sand, silt and clay. Sediment supply is primarily marine in origin, compared to other salt marshes which are usually formed from river-born sediments. The upper limit of the salt marsh forms
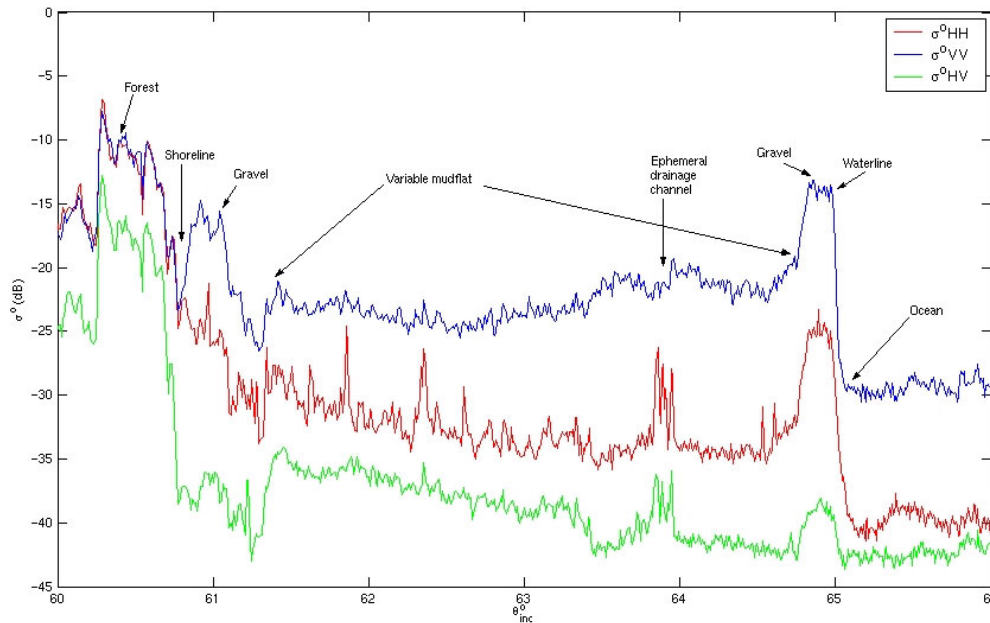
FIGURE 9: Plot of backscatter values along a portion of the Evangeline mudflat. Relative locations of different geomorphic targets have been verified during field visits. Backscatter transect denoted in Figure 6. Curves derived from averaging in azimuth by 200 samples per line.

the highest high water line and the lower limit forms the mean sea level. Salt marshes form a large component of the intertidal zone in the southern Bight of the Minas Basin (e.g., Cornwallis, Canard, Habitant). These marshes are separated into a lower marsh dominated by *Spartina alterniflora* and a high marsh dominated by *Spartina patens*. Other plants present include angiosperms, algae and microscopic fungi.

**A**   **B**
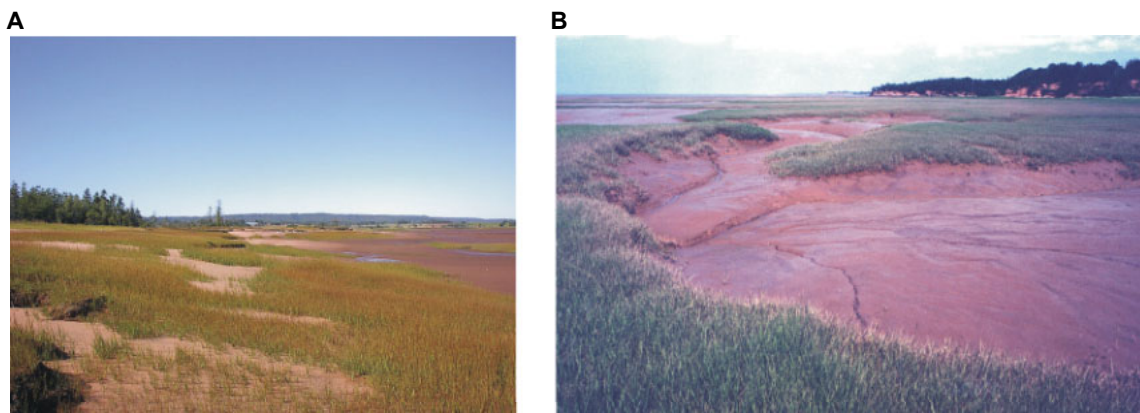
FIGURE 10: A) Photograph of patchy marsh vegetation with sandy substrate near Starr's Point, B) muddy substrate at Canard River.

The multi-polarization composite image reveals several important characteristics of the salt marshes, particularly spatial variations in the nature of the substrate (Figure 7). High radar return areas are found along the lower marsh near the mudflats. Field reconnaissance indicates that these areas have patchy vegetation and sandy soils (Figure 10A). Darker

areas are observed in the high marsh regions where the substrate is smoother and primarily composed of saturated silt and mud (Figure 10B).

Comparison of the three polarization power images does not reveal any significant difference in the backscatter from the salt marshes however there is considerable difference in some of the adjacent agricultural fields and forests, and along the banks of the Canard River. The main difference between the images occurs because of multiple reflections from different vegetation types which result in depolarization and subsequently a higher backscatter in the cross-polarized channel.

Examination of the backscattered power along a transect across the Canard and Habitant River Estuaries reveals the effect of the salt marsh vegetation on the sigma naught values (Figure 11). All three polarizations have high values over the marsh which drop significantly over the bare surface of the tidal channels, dropping most for the HH- and HV-polarizations. In the marsh vegetation, the backscatter from the HH-polarization is generally higher than that from VV because of the improved penetration of the horizontally polarized electromagnetic waves into the vertically oriented marsh vegetation, and because the vertically polarized waves couple more effectively with the vegetation resulting in increased attenuation.
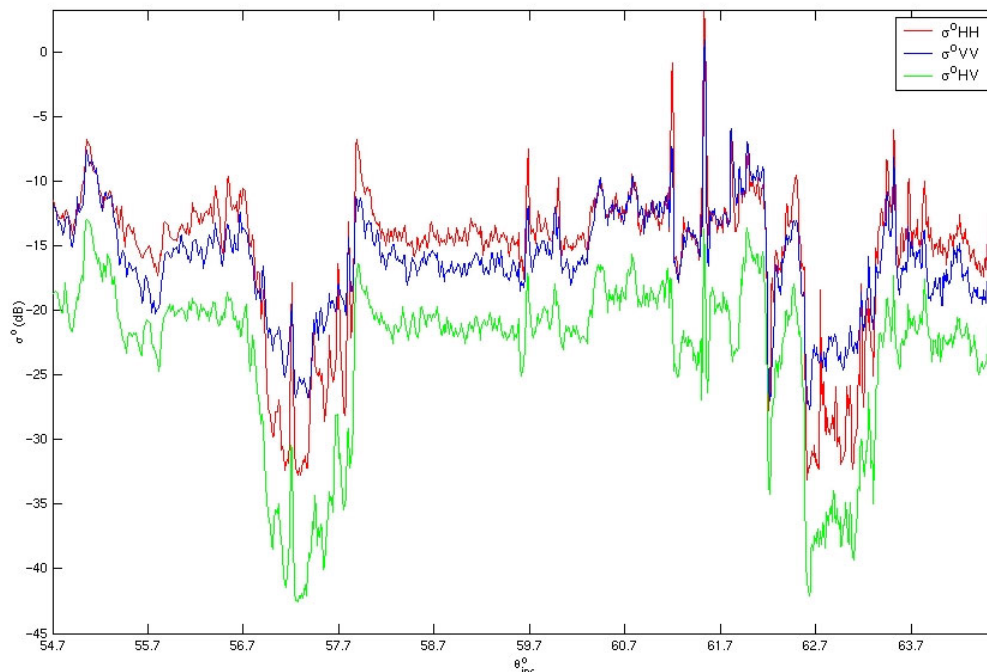
FIGURE 11: Plot of backscatter values along a portion of the salt marshes. The two sharp increases in the backscatter (i.e., -0.9 and 3.6 dB) are associated with reflection from metallic roofs of a poultry farm. Backscatter transect denoted in Figure 7. Curves derived from averaging in azimuth by 200 samples per line.

6.5 Mudflats of the Canard and Habitant Estuaries

Extensive mudflats are found at the mouths of the Canard and Habitant Estuaries. The mudflats are dissected by numerous dendritic tidal creeks which have cut into the soft marine deposits. Wave action is minimal and sediment transport is largely controlled by tidal currents (Amos et al., 1988). The mudflat is biologically very active and a key feeding ground for foraging shore birds. The flat off Starr's Point has been studied extensively by Amos et al. (1988) for variations in the sediment bulk properties when exposed at low tide.

The authors noted a gradual seaward sediment gradation across the flat from fine to coarse. Bedforms are limited to the periphery of the flat.

The multi-polarization image of the mudflats is shown in Figure 8. Tidal creeks are clearly visible on the image. The red streaks in the image are the result of system artifacts. Superimposing the relative location of the transect by Amos et al. (1988) shows that there is some similarity between the brightness of the power images and the gradation of sediment from fine to coarse. Backscatter values support these observations and show that there is considerably higher return from the sand in all three polarizations when compared to mud. Comparison of the amplitude images for the three polarizations shows that the two horizontal transmit polarization images provide the best contrast for discriminating tidal creeks whereas the high return in the VV-polarization due to surface roughness (i.e., sand) reduces discrimination in some areas.

7. TERRAIN POLARIZATION RESPONSE STATISTICS

In this section, various terrain polarization response statistics are evaluated for eleven distinct geomorphic targets: water, mud, sand, silty-sand, gravel, bedrock, salt marsh with muddy substrate, salt marsh with sandy substrate, forest, small ripples, and megaripples. Analysis involved the extraction of polarization response plots and statistics. The statistics are sigma naught for the three linear polarizations (σ^o_{HH}, σ^o_{HV}, σ^o_{VV}), co-polarized phase difference ($\Phi_{HH - VV}$), co-polarized pedestal height, total power (Stokes matrix element M_{11}), co-polarized ratio (HH/VV), and cross-polarized ratio (HH/HV).

Polarization response plots are graphical representations of the variation of co- or cross-polarization radar returns as they are distributed over half of the Pointcaré sphere (Boerner et al., 1998). These diagrams are used to support the identification of the target scattering mechanism. The backscatter range along the vertical axis is normalized between 0.0 and 1.0. The horizontal axes contain the orientation and ellipticity angles (0º to 180º and –45º to 45º respectively). The pedestal height provides a measure of the unpolarized return, which in turn provides a measure of the degree of volume scattering and relative roughness of the selected area (van Zyl et al., 1987). Total power (SPAN) is the sum of the four linear polarizations (eq. 7a) and is related to the roughness of the target relative to the radar wavelength (Small and Cummings, 1991). The co- (HH/VV) and cross-polarized ratios (HH/HV) measure the strength of the differences between the HH and VV returns and HH and HV returns, respectively. Values approaching 1.0 indicate random target structure. The co-polarized phase difference provides a measure of the type of scattering (close to 0 for single bounce, 180 for double bounce and variable for multiple interactions).

Since ground data were unavailable during the CV580 image acquisition over Minas Basin, two approaches were taken in order to avoid ambiguities in the interpretation of the polarization response statistics and hence, in distingushing different intertidal terrain types. The approaches involved a qualitative integration of ancillary data from air photos and field observations. The initial task consisted of delineating broad groups of intertidal terrain types on air photos (1960-1995). Most of these areas were then field checked in June and August 2001 in order to: a) identify training areas which had a consistent distribution of surface roughness and moisture, and b) better understand the sediment composition. Once training areas were identified, the polarization response statistics were calculated for sample sizes containing no less than 5500 pixels in order to ensure a statistically robust sample.

7.1 Polarimetric parameters

The polarimetric statistics derived for various geomorphic targets are summarized in Table 1. The sigma naught values show that the cross-polarized backscatter was consistently lower than the linear polarizations. Backscatter from HH exceeded VV for gravel, silty sand and mud. The lowest cross-pol backscatter occurred from water (-44.56) and mud (-40.92). Bedrock, forest, gravel, sand, high marsh and low marsh produced high returns in all three polarizations. The best contrast between water and the sediments was in the HH-pol. Large differences in the return from the cross-polarized and linear polarizations (> 15 dB) occur for megaripples and silty sand, indicating little depolarization of the incident wave. With the exception of sand, σ°_{VV} decreases as particle size decreases. One possible reason why sand has a higher backscatter than gravel is because the surface of the sand may have been roughened by human disturbance (the location chosen for the polarimetric response of sand is commonly roughened by people walking on it). Backscatter values from the vegetation classes are very similar, however σ°_{HH} is higher from the forest (deciduous) compared to the vertically oriented marsh vegetation. It should be pointed out that σ°_{HH} and σ°_{HV} from the deciduous forest are nearly equal, highlighting the importance of volume scattering. HH backscatter provided the best contrast between the high and low marsh sub-environments, reflecting the effects of the sandy substrate (low marsh) which is rougher than the muddy substrate characteristic of the high marsh sub-environment.

Target	Sample size (pixels)	Inc. Angle (°)	Co-pol Pedestal height	Co-polarized ratio	Cross-polarized ratio	Co-polarized phase difference	σ_{HH} (dB)	σ_{VV} (dB)	σ_{HV} (dB)	Total power (dB)
Water	7420	63.7	0.08	0.12	0.30	18.43	-39.39	-30.20	-44.56	-35.45
Bedrock	5911	64.5	0.47	1.31	0.13	20.64	-12.89	-14.05	-21.80	-15.85
Small ripples	7088	61.8	0.11	0.17	0.17	23.51	-30.36	-22.61	-37.96	-27.75
Mega ripples	12526	66.9	0.26	0.85	0.04	36.14	-19.82	-19.13	-34.32	-22.34
Deciduous forest	13295	60.4	0.56	1.01	0.21	5.65	-10.40	-10.46	-17.14	-12.60
Gravel	8775	60.9	0.38	0.72	0.10	48.16	-13.66	-12.24	-23.57	-15.54
Sand	6314	65.2	0.55	1.36	0.15	20.93	-11.16	-12.49	-19.32	-14.08
Silty sand	15619	59.4	0.23	0.47	0.06	27.50	-23.05	-19.82	-35.09	-23.98
Mud	12651	61.4	0.21	0.39	0.09	45.53	-30.36	-26.31	-40.92	-30.68
Salt marsh/mud	11957	61.2	0.45	1.34	0.29	14.05	-15.01	-16.28	-20.34	-17.35
Salt marsh/sand	8893	61.0	0.39	2.33	0.13	-8.66	-10.57	-14.25	-19.28	-14.29

TABLE 1: Polarimetric parameters for geomorphic targets in the intertidal zone.

The SPAN or total power had a wide range of values among the different geomorphic targets. Values of total power reflect the micro-scale roughness of the individual targets. High values of total power occur for bedrock, forest, gravel, sand and salt marsh (sandy substrate). Low values occur for smoother surfaces such as water, silty sand, mud and the bedform classes. The co-polarization phase difference values indicate that the return from forest and salt marsh with sandy substrate are very similar, with the vertical phase being slightly smaller than the horizontal phase for the marsh (i.e., negative values). Co-pol phase difference from other targets shows that the horizontal phase is consistently greater than the vertical phase. Pedestal height values were high (0.38 to 0.56) for bedrock, forest, gravel, sand, and the two salt marsh classes. This range is similar to forest targets reported by Zebker and van Zyl (1991). The high pedestal height for sand indicates that it may have experienced some volume scattering in addition to multiple scattering, whereas the high pedestal for gravel and bedrock is likely attributable solely to

multiple reflections. The co-polarization ratios show significant difference in the linear polarization returns. The largest difference occurs for the salt marsh with sand substrate, because the horizontally polarized waves are more effective at penetrating the vertically oriented marsh vegetation, and because the vertically polarized waves couple more effectively with the vegetation resulting in increased attenuation. Ratios above unity also occur for rough surfaces such as bedrock, forest, sand and high marsh. In contrast, low co-pol ratios occur for smoother surfaces such as water, mud, and silty sand.

The effect of the co-polarization ratio can be seen clearly in the polarization response plots (APPENDIX 2). For comparative purposes these plots were derived from a narrow incident angle range (60-67º). Also, the response from a dihedral corner reflector deployed at Minas Basin is included. The distinct saddle shape produced in the response plots for bedrock, sand, both salt marsh classes, and forest confirms the dominance of $\sigma°_{HH}$. This response is typical of double bounce reflection. There is a noticeable increase in the HH component with increasing grain size. The exception to this trend is sand because it is rougher than the other sediments possibly as a result of human-induced roughening. The peak in the response from the marsh with muddy substrate is somewhat offset from an ideal HH response with orientation angle at $3°$. This offset indicates that there is a peak return from a wave oriented a few degrees off the horizontal axis. Comparison of the polarization responses derived from the different intertidal sub-environments with theoretical responses indicates several different scattering mechanisms (APPENDIX 3). None of the targets produce responses similar to a smooth dielectric surface. The responses from bedrock, sand, and both salt marsh classes are comparable to the theoretical response of a dihedral corner reflector. The response from water, mud, silty sand and gravel are comparable to the response from a rough surface. Notice in APPENDIX 2 that the horizontal polarization contribution increases progressively from water to mud, silty sand and then gravel. Ideally, the response from sand should lie somewhere between that of silty sand and gravel.
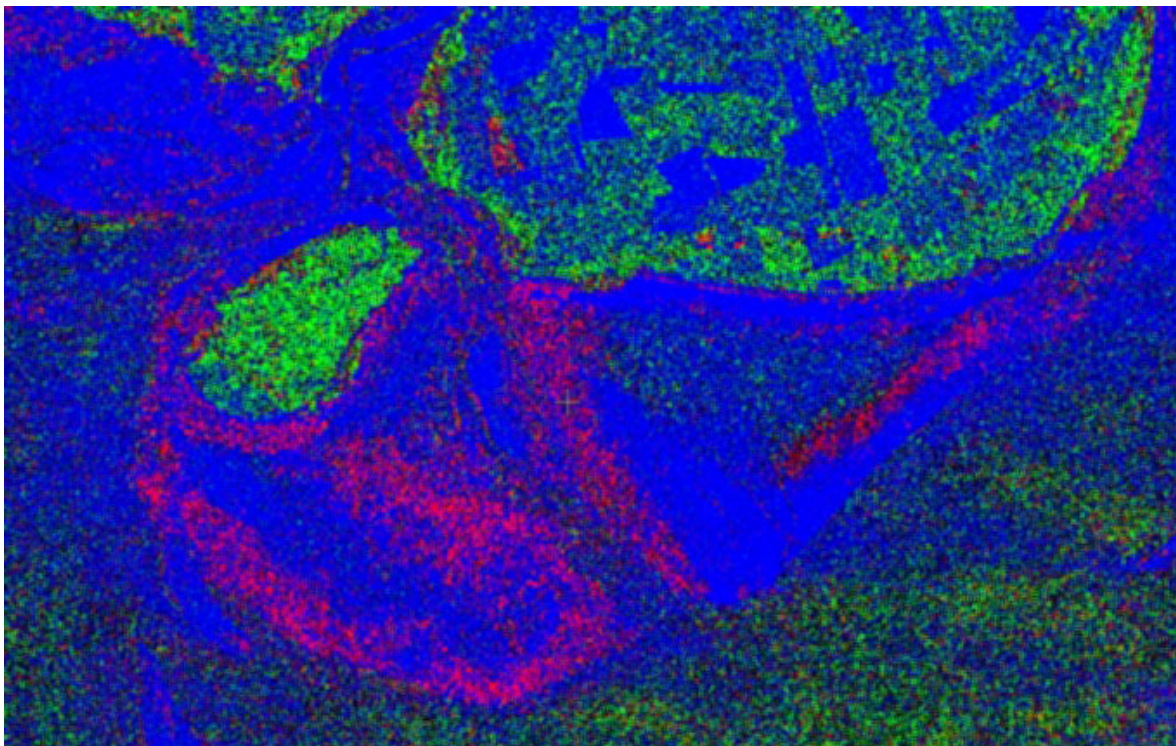
7.2 Unsupervised classification

In addition to the polarization response analysis, an unsupervised classification was performed using the method outlined by van Zyl (1989). The method classifies the dominant scattering behaviour of each pixel by comparing the polarization properties of each pixel to one of three scattering classes: double bounce scattering, diffuse scattering and odd bounce scattering. Results from the analysis are shown in Figures 12A and B. The classifications show good agreement with the known distribution of gravel deposits (double bounce), mud deposits (odd bounce -- single bounce), marsh vegetation and forest (diffuse scattering). The classification results over water are not valid since the algorithm assumes the target to be reciprocal. It should be pointed out that the bright area along the western margin of Middle Ground sandbar (see section 6.1), previously explained as either Bragg scattering or scattering from boulders, is classified as double bounce, confirming that the high backscatter is from boulders. Overall, the results from the unsupervised classification add considerable support in identifying the scattering mechanism and for identifying different tidal sub-environments.

8. CONCLUSIONS

High-resolution fully polarimetric SAR data can provide an excellent source for the identification and delineation of geomorphic targets in the intertidal zone. The findings presented here indicate that polarimetric SAR data can be used to delineate various intertidal sediment and vegetation classes according to their scattering response. The

A

B
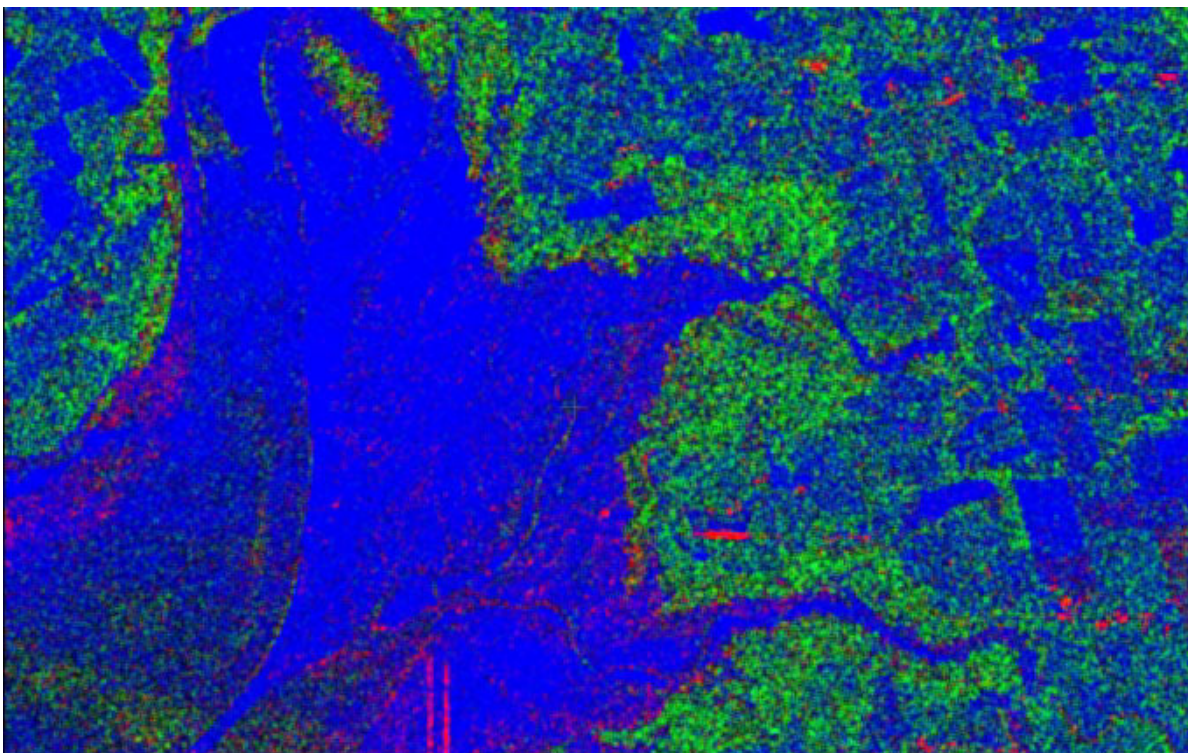
FIGURE 12: Unsupervised classification results using van Zyl (1989) method (Red = double bounce, Green = diffuse scatter, Blue = odd bounce) for A) Evangeline mudflat and B) Canard and Habitant salt marshes.

results from an unsupervised classification indicate that polarimetric SAR data are useful for classifying intertidal terrain where different scattering mechanisms are present. In addition to the enhanced target information, a preliminary analysis of backscatter variations from different surface types indicates that the HH and cross-polarized channels provide excellent sources for delineating the mean high water line or shoreline. The improved shoreline mapping potential of these channels is the result of high backscatter contrasts between land targets and low return from both water and the intertidal zone. Collectively these results suggest some improvement in the potential of the fully polarimetric modes of RADARSAT-2 for coastal mapping.

9. RECOMMENDATIONS

The findings presented here provide some insight into the information content of polarimetric SAR for geomorphic mapping in the intertidal zone of macro-tidal basins. However, only a limited portion of the fully polarimetric CV580 SAR data were examined in this study and attempts should be made to examine other polarimetric methods for mapping various geomorphic targets and delineating the shoreline vector. Recent advances in polarimetric SAR filtering and classification should be examined in order to identify the optimum method for classifying geomorphic targets in the intertidal zone and extracting the most accurate shoreline vector. Of particular interest are methods developed by Lee et al. (1999), Cloude and Pottier (1997), and Yeremy et al. (2000). These methods should be examined from different coastal areas in order to compare the POL-SAR data from a range of geomorphic settings. In addition, further studies should be undertaken to explore the scattering properties of intertidal sediments and coastal vegetation in order to build a comprehensive understanding of scattering response from these sub-environments.

10. REFERENCES

Amos, C.L., N.A. Van Wagoner, and G.R. Daborn, The influence of subaerial exposure on the bulk properties of fine-grained intertidal sediment from Minas Basin, Bay of Fundy, *Estuarine, Coastal Shelf Science*, **27**: 1-13, 1988.

Bartholdy, J., and S. Folving, Sediment classification and surface type mapping in the Dannish Wadden Sea by remote sensing, *Netherlands Journal of Sea Research*, **20**: 337-345, 1986.

Bell, W.A., Mississipian Horton Group Of Type Windsor-Horton District, Nova Scotia, Department of Mines and Technical Surveys Canada, 1960.

Bousfield, E.L., and A.H. Leim, The fauna of the Minas Basin and Minas Channel, *Bulletin of the National Museum of Canada*, **166**: 1-30, 1960.

Boerner, W.M., H. Mott, E. Luneburg, C. Livingstone, B. Brisco, R.J. Brown, and S. Paterson, Polarimetry in Radar Remote Sensing: Basic and Applied Concepts*, In: Henderson, F.M. and A.J. Lewis,* Manual of Remote Sensing*, 3rd Edition, Vol.* **2**, 271-357, 1998.

Canadian Hydrographic Service, Avon River and approaches; Chart 4140, 1972.

Cloude, S.R., and E. Pottier, An entropy based classification scheme for land applications of polarimetric SAR image data, *IEEE Transactions on Geoscience and Remote Sensing*, **35**: 68-78, 1997.

Hawkins, R.K., R. Touzi, and C.E. Livingstone, Calibration and use of CV-580 airborne polarimetric SAR data, *Proceedings of the Fourth International Airborne Remote Sensing Conference and Exhibition / 21st Canadian Symposium on Remote Sensing*, **2**: 32-40, 1999.

Knight, R.J., and R.W. Dalrymple, Winter conditions in a macrotidal environment, Cobequid Bay, Nova Scotia, *Geographie Physique et Qauternaire*, **3**(1-2): 65-85, 1076.

Lambiase, J.J., Topographic control of sediment distribution on an intertidal sand bar: a case study, *In: McCann, S.B., The Coastline of Canada: Littoral processes and chore morphology, GSC Paper 80-10*, 181-187, 1980.

Lee, J.S., M. R. Grunes, T. L. Ainsworth, Li-Jen Du, Dale L. Schuler, and S. R. Cloude. Unsupervisied Classification Using Polarimetric Decompostion and the Complex Wishart Classifier. *IEEE Transactions on Geoscience and Remote Sensing,* **37**(5): 2249-2258, 1999.

Livingstone, C.E., A.L. Gray, R.K. Hawkins, P. Vachon, T.I. Lukowski, and M. Lalonde, The CCRS airborne SAR systems: Radar for remote sensing research, *Canadian Journal of Remote Sensing*, **21**(4): 468-491, 1995.

Lohani, B., and D.C. Mason, Extraction of tidal channel networks from LiDAR data, *Proceedings of the Fourth International Airborne Remote Sensing Conference and Exhibition / 21st Canadian Symposium on Remote Sensing*, **1**: 672-679, 1999.

Melsheimer, C., G. Tanck, M. Gade, and W. Alpers, Imaging of tidal flats by the SIR-C/X-SAR multi-frequency / multi-polarization synthetic aperture radar, *In: Nieuwenhuis, G.J.A., R.A. Vaughan, and M. Molenaar, Operational Remote Sensing for sustainable development: Proceedings of the 18th EARSel Symposium on Operational Remote Sensing for Sustainable Development, Enschede, Netherlands, May 11-14*, 189-192, 1998.

Middleton, G.V., Crief Field Guide to Interidal Sediments, Minas Basin, Nova Scotia, *Maritime Sediments*, **8**(3): 114-122, 1972.

Rainey, M.P., A.N. Tyler, R.G. Bryant, D.J. Gilvear, and P. McDonald, The influence of surface and interstitial moisture on the spectral characteristics of intertidal sediments: implications for airborne image acquisition and processing, *International Journal of Remote Sensing*, **21**(16): 3025-3038.

Small, D., and I. Cumming, Evaluation study on multi-frequency polarimetric SAR, Final Report, p.102, 1991.

Swift, D.J.P., and R.M. McMullen, Preliminary Studies of Intertidal Sand Bodies in the Minas Basin, Bay of Fundy, Nova Scotia*, Canadian Journal of Earth Sciences*, **5**(2): 175-183, 1968.

Tanck, G., W. Alpers, and M. Gade, Determination of surface roughness parameters of tidal flats from SIR-C/X-SAR 3-frequency SAR data, IGARSS '99, 1677-1679, 1999

Thomas, M.L.H., Intertidal Resources of the Bay of Fundy, *In: Daborn, G.R., Fundy Tidal Power and the Environment: Proceedings of the Environmental Implications of Fundy Tidal Power, Wolfville, Nova Scotia, November 4-5,* 148-159, 1977.

Tittley, B., The Analysis and Interpretation of SAR Imagery Applied to Intertidal Zone Geomorphology, Unpublished Co-Operative Project Thesis, Nova Scotia College of Geographical Sciences, Lawrencetown, NS., 42p, 1990.

Tittley, B., and D. Werle. Using RADARSAT-1 SAR Imagery for Coastal Zone Sensitivity Mapping in Nova Scotia, AERDE Environmental Research, Halifax, Nova Scotia, EOP3 Contract 234-13-5 D550, 72p, 1997.

van Zyl, J.J., Unsupervised classification of scattering behavior using radar polarimetry data, *IEEE Transactions on Geoscience and Remote Sensing*, **27**: 36-45, 1989.

van Zyl, J.J., and H.A. Zebker, Imaging Radar Polarimetry*, In: J.A. Kong,* Progress in Electromagnetics Research, Pier 3, 277-370, 1990.

van Zyl, J.J., H.A. Zebker, and C. Elachi, Imaging radar polarization signatures: Theory and observation, *Radio Science*, **22**(4): 529-543, 1987.

Yates, M.G., A.R. Jones, S. McGrorty, and J.D. Goss-Custard, The use of satellite imagery to determine the distribution of intertidal surface sediments of the Wash, England, *Estuarine, Coastal and Shelf Science*, **36**: 333-344, 1993.

Yeo, R.K., and M.J. Risk, The Sedimentology, Stratigraphy, and Preservation of Intertidal Deposits in the Minas Basin System, Bay of Fundy, *Journal of Sedimentary Petrology*, **51**(1): 245-260, 1981.
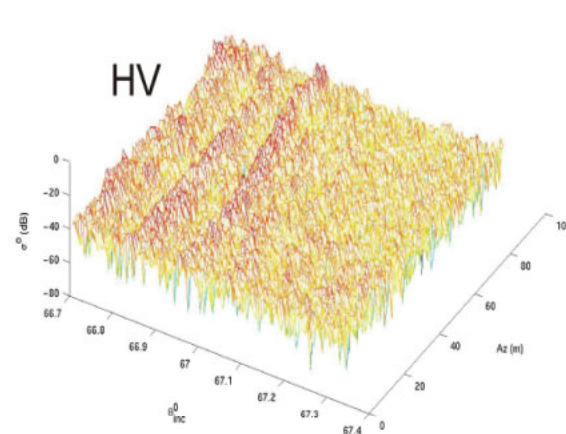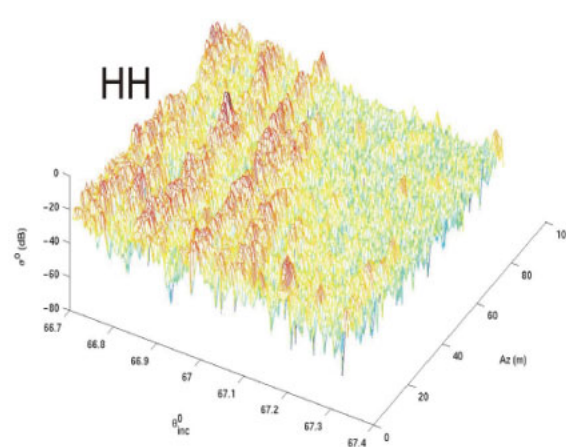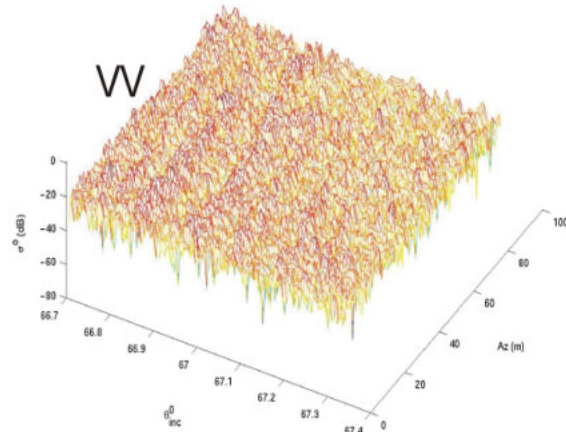
Yeremy, M., J. D. Beaudoin, G. M. Walter, and A. Beaudoin, Shoreline mapping from SAR imagery: a polarimetric approach*, Proceedings of the 22nd Canadian Symposium on Remote Sensing*, 365-374, 2000.

Zebker, H.A, and J.J. van Zyl, Imaging Radar Polarimetry: A Review, *Proceeding of the IEEE*, **79**(11): 1583-1606, 1991.
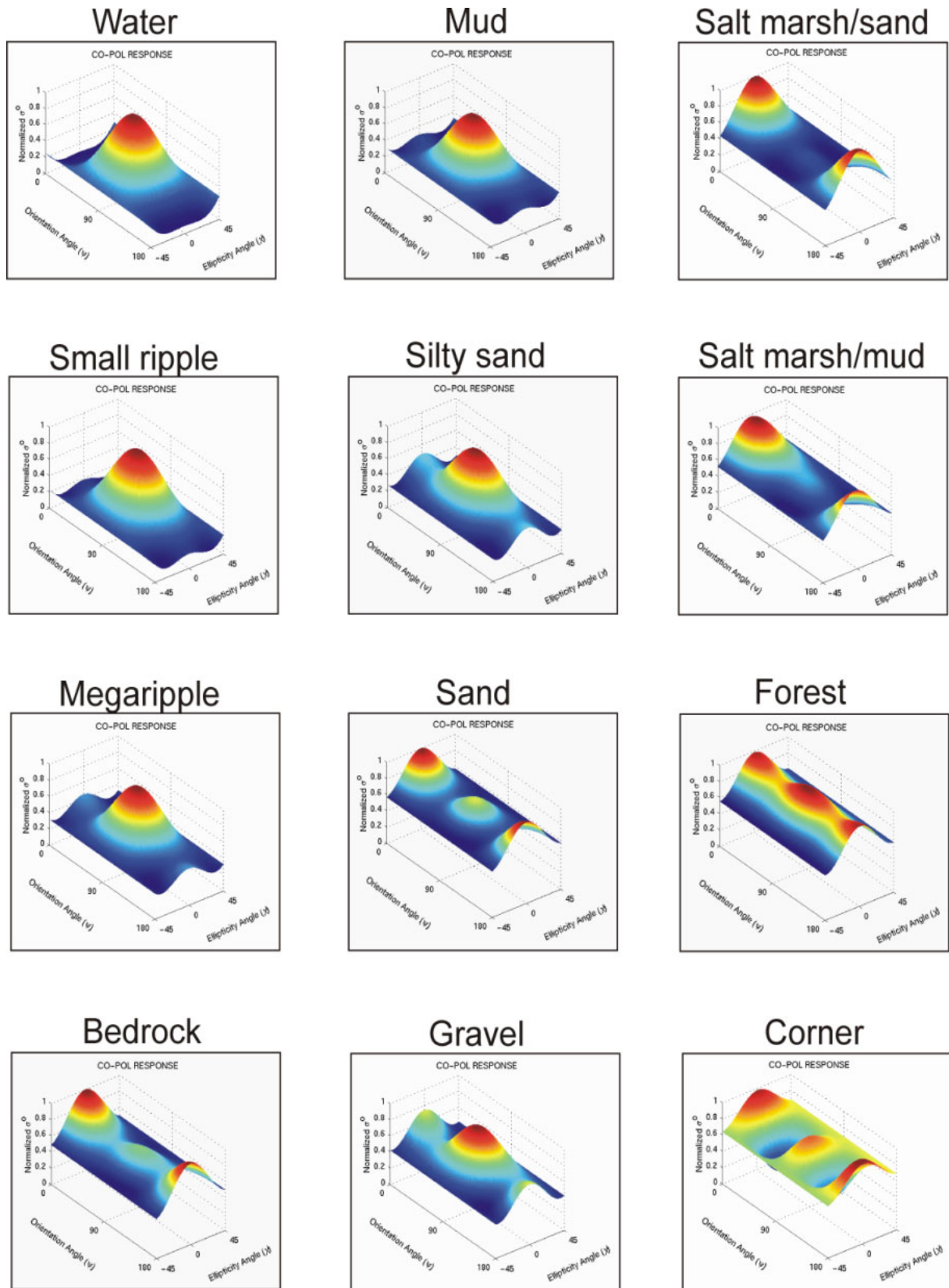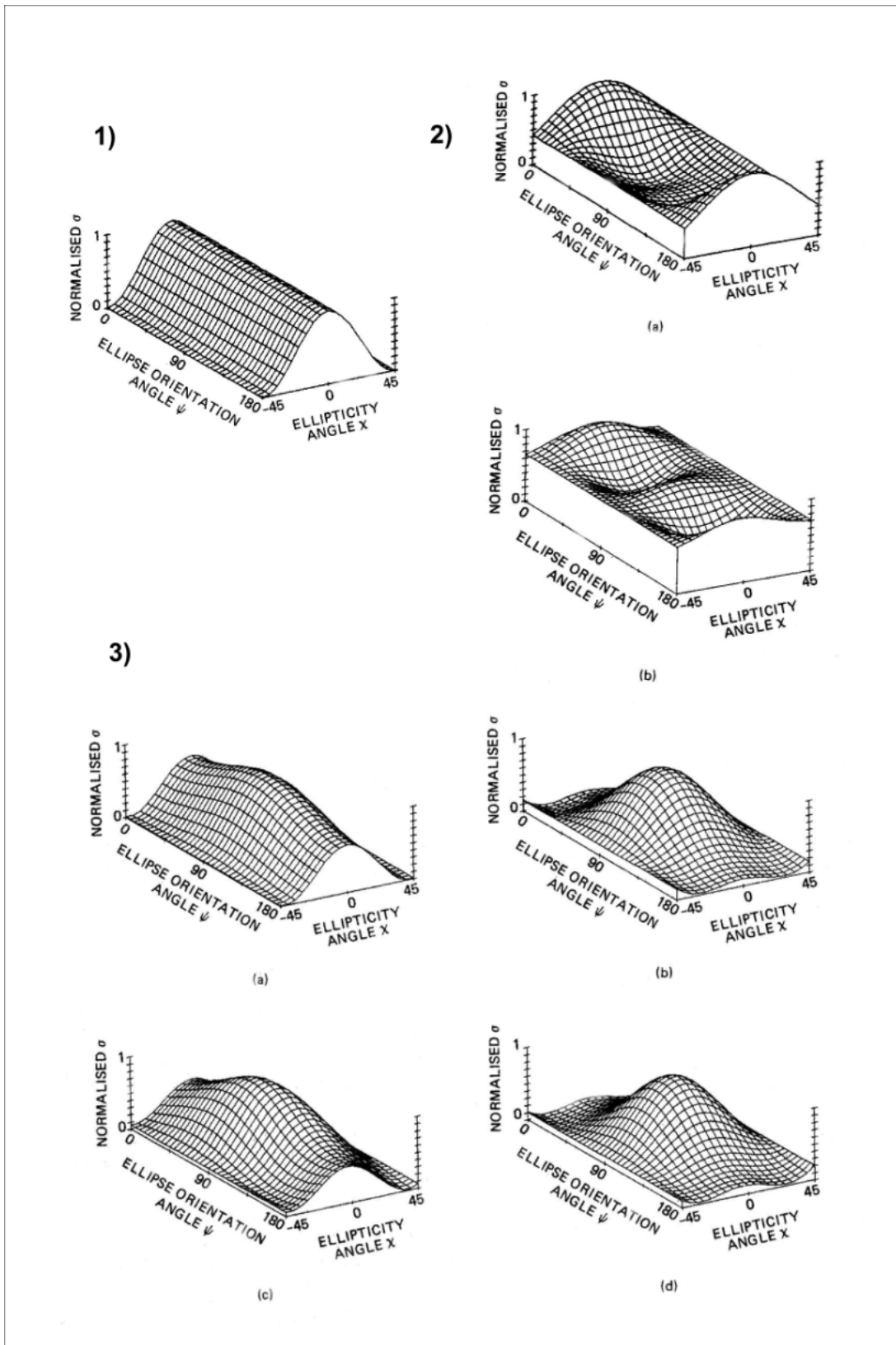
A
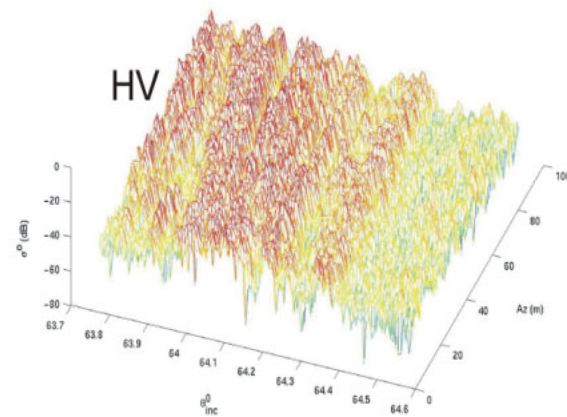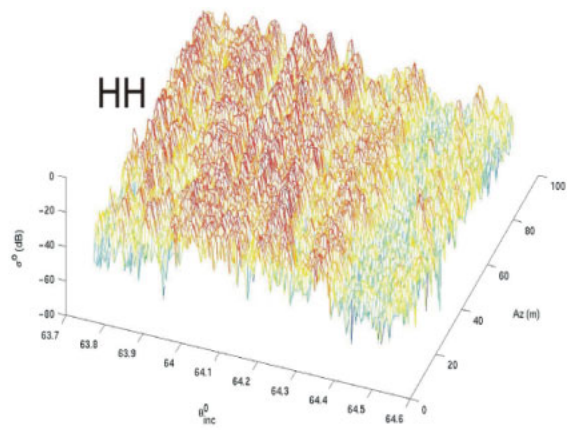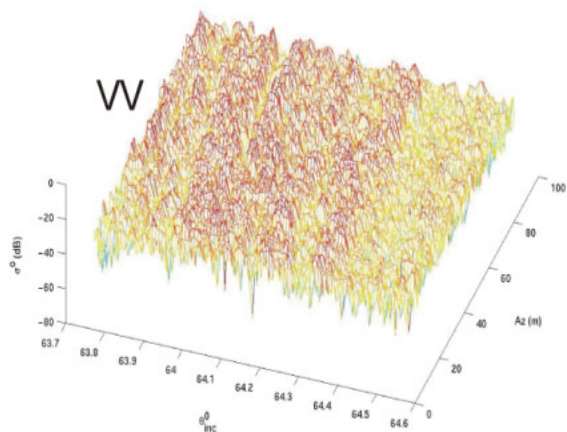
B

APPENDIX 1: Three-dimensional plots of backscatter from A) megaripples on Middle Ground sandbar and B), modulated bedrock surface at Scotch Rocks.

APPENDIX 2: Polarization response plots for various geomorphic targets. Polygons used to derive the plots contained no less than 5500 samples and were taken from incident angles ranging from 60-67°.

APPENDIX 3: Polarization response plots from van Zyl et al. (1987) showing: (1) a smooth dielectric surface, (2a) a modelled response from a dihedral corner reflector, (2b) an actual corner reflector, (3a) a modelled rough surface at 20º incident angle, (3b) rough ocean surface at 20º incident angle, (3c) modelled rough surface at 50º incident angle, and (3d) rough ocean surface at 50º incident angle.